Journal of Geophysical Research: Oceans

RESEARCH ARTICLE
10.1029/2018JC013960

Key Points:
- Fifty-day oscillation signals in the Celebes Sea exhibit intense interannual modulations
- Southward migration of wind-driven tropical and subtropical gyres is inductive to enhanced 50-day oscillations inside CS
- Amplitude of the 50-day oscillation in the CS affects water mass properties of ITF; enhanced 50-day oscillation lowers ITF's salt content

Correspondence to:
X. Chen,
chenxiao1231@hhu.edu.cn

Citation:
Chen, X., Qiu, B., Chen, S., Cheng, X., & Qi, Y. (2018). Interannual modulations of the 50-day oscillations in the Celebes Sea: Dynamics and impact. *Journal of Geophysical Research: Oceans*, *123*, 4666–4679. https://doi.org/10.1029/2018JC013960

Received 8 MAR 2018
Accepted 1 JUN 2018
Accepted article online 12 JUN 2018
Published online 5 JUL 2018

Interannual Modulations of the 50-Day Oscillations in the Celebes Sea: Dynamics and Impact

Xiao Chen[1], Bo Qiu[2], Shuiming Chen[2], Xuhua Cheng[1], and Yiquan Qi[1]

[1]College of Oceanography, Hohai University, Nanjing, China, [2]Department of Oceanography, University of Hawai'i at Mānoa, Honolulu, HI, USA

Abstract Intense 50-day oscillations have been previously observed at the entrance of Celebes Sea, and their formation has been suggested to be a result of Rossby wave resonance where the frequency of cyclonic eddy shedding by the intruding Mindanao Current matches that of the gravest Rossby mode of the semienclosed Celebes Sea basin. Using the ocean state estimate of 1993–2016 from the Estimating the Circulation and Climate of the Ocean, Phase II, we detected strong interannual modulations in the shedding of cyclonic eddies at the Celebes Sea entrance. Active eddy sheddings occurred during 1993, 2002–2003, 2006–2010, and 2013–2015. Southward shifting of the wind-driven North Pacific tropical gyre and the concurrent strengthening of the Mindanao Current southeast of the Mindanao Island in these years are found to be inducive for the generation of cyclonic eddies intruding into the Celebes Sea. Modulated by the activity of eddy sheddings, the upper ocean water mass properties in both the Celebes Sea and Makassar Strait exhibit noticeable interannual changes with less saline waters appearing in the 75- to 175-m layer during the active eddy shedding years.

1. Introduction

The Celebes Sea (CS), also known as the Sulawesi Sea, is a choke point where the western Pacific Ocean circulation and water masses are connected and intermingled to those in the eastern Indian Ocean. It constitutes the formation area for the Indonesian Throughflow (ITF) that controls the heat and freshwater balance of the Indian Ocean and is along the pathway of the global conveyor circulation (e.g., Broecker, 1991; Fine et al., 1994; Gordon, 1986, 2005). The oceanic circulation in the CS is subject to multiple factors. Located at the western end of the tropical Pacific Ocean, the CS is where westward-propagating interior oceanic variability of various sources accumulates. The strong air-sea interaction surrounding the Maritime Continent exposes the CS to intense regional wind forcing of monsoons and Madden-Julian Oscillations (Madden & Julian, 1994; Zhang, 2005). In addition to the atmospheric wind forcing, the CS is also at the crossroads of equatorial and coastal waveguides of the Pacific, the Indian, and the neighboring marginal seas (e.g., Gordon et al., 2012; Potemra, 2001; Sprintall et al., 2000; Wijffels & Meyers, 2004; Zhuang et al., 2013), subjecting it to oceanic variability of remote origins. Finally, the unique geometry of the CS basin, being approximately rectangular in shape, can work to amplify oceanic variability through resonance (Masumoto et al., 2001; Qiu et al., 1999).

Because of the multiple factors listed above, the CS circulation can fluctuate over intraseasonal, annual, interannual, and longer time scales. Numerous observational, numerical, and theoretical studies in the past have examined the regional circulation fluctuations around the Indonesian Archipelagos with the focus often on the temporal changes of ITF. Indeed, our understanding of the ITF changes in the Makassar Strait and the ITF exit straits into the Indian Ocean over the seasonal and longer time scales has improved significantly in the past two decades, thanks to sustained in situ measurements by numerous international programs (for a comprehensive review, see Sprintall et al., 2014).

Compared to that within and downstream of the Makassar Strait, ocean circulation variability of the upstream ITF inside the CS is less adequately explored. This is so because in situ measurements inside the CS are rare and satellite altimetry measurements, which have been utilized broadly in regions where in situ measurements are lacking, have issues of tide aliasing in marginal seas such as the CS. (The TOPEX/Poseidon and its subsequent Jason satellite missions have repeat cycle of 9.9156 days. This repeat cycle aliases the semidiurnal M_2 tides, for example, into the 62.1-day altimeter-derived sea surface height [SSH] signals [Ray, 1998].) A 14-month-long current meter mooring measurement was conducted by Kashino et al. (1999) at

the Pacific entrance of the CS near 4°N and 127.5°E. Throughout the mooring duration, persistent 50-day flow oscillations were detected at the depths of 350 and 550 m. The observed flow fluctuations at these two depths tended to be out of phase, suggesting the baroclinic nature of the observed 50-day oscillations. Using mooring observations inside the Makassar Strait, Susanto et al. (2000) and Pujiana et al. (2009) have noted elevated intraseasonal variability in the observed along-strait velocity data. Possible impact from both the CS variability and the eastern Indian Ocean Kelvin waves was suggested. Within the Indonesian Seas, Napitu et al. (2015) analyzed recently the weekly sea surface temperature (SST) data from the Tropical Rainfall Measuring Mission Microwave Imager satellite of 1998–2012 and found elevated SST changes in the intraseasonal frequency band of 21–119 days. While the broadbanded intraseasonal signals are detected in all subregions of the Indonesian Seas, the SST variability inside the CS was found to have a relatively narrow spectral peak centered at 56 days, whose characteristics are different from those in the Banda and Timor Seas. Rather than forced by the Madden-Julian Oscillation-related wind forcing, the intraseasonal SST signals in the CS are hypothesized by Napitu et al. (2015) to be likely caused by regional oceanic processes.

To clarify the dynamical processes responsible for the observed 50-day oscillations inside the CS, Qiu et al. (1999) conducted a series of process-oriented numerical model experiments by varying coastline geometry and surface wind forcing. Based on these experiments, they showed that the enhanced 50-day oscillations in the CS are a result of baroclinic Rossby wave resonance in which the frequency of flow oscillation

$$\omega = \frac{\beta}{2}\left(\frac{n^2\pi^2}{{L_x}^2} + \frac{m^2\pi^2}{{L_y}^2} + \frac{f^2}{g'h}\right)^{-1/2} \tag{1}$$

is dictated by the gravest Rossby mode of the semienclosed CS basin. In equation (1), L_x and L_y are zonal and meridional lengths of the CS basin, respectively; f is the Coriolis parameter; β is the meridional gradient of f; $g'h$ is the squared baroclinic gravity wave speed; and n and m are mode numbers in the x and y directions, respectively. For parameter values appropriate for the CS, L_x = 720 km, L_y = 500 km, $g'h$ = 9.1 m^2/s^2, $f = 1.02 \times 10^{-5}{\cdot}s^{-1}$, and $\beta = 2.3 \times 10^{-11}{\cdot}m^{-1}{\cdot}s^{-1}$, the gravest basin Rossby mode ($n = m = 1$) has a resonant wave period of 52.8 days.

While our basic understanding of the 50-day oscillations inside the CS is established, lack of sustained long-term observations has precluded studies in the past to examine the interannual changes of the intraseasonal oscillations inside the CS. To overcome this situation, we use in this study the ocean state estimate of 1993–2016 from the Estimating the Circulation and Climate of the Ocean, Phase II (ECCO2). Since it is constructed in a dynamically and thermodynamically consistent way (see section 2) and produced adequately the intraseasonal eddy variability inside the CS, the ECCO2 state estimate is well suited to explore the interannual modulations of the CS 50-day oscillations.

There are three objectives in our study. First, we strive to quantify the interannual modulations of the intraseasonal eddy variability inside the CS by introducing an appropriate index. Dynamical processes responsible for the detected interannual modulations are examined next. Finally, we discuss the impact of the interannual modulations of the CS intraseasonal variability upon the water mass properties of the ITF.

2. ECCO2 State Estimate and Archiving, Validation, and Interpolation of Satellite Oceanographic SSH Data

The ECCO2 simulation is based on the three-dimensional hydrostatic and Boussinesq global ocean model of the Massachusetts Institute of Technology general circulation model (Marshall et al., 1997). The model has a mean horizontal resolution of 18 km and 50 vertical levels with varying resolution from 10 m near the surface to 456 m near the ocean bottom. The eddy-permitting ocean state estimate is obtained by a least squares fit of the Massachusetts Institute of Technology general circulation model to available satellite observations and in situ measurements. Using the optimized parameters (e.g., initial temperature-salinity conditions, background eddy diffusivity and viscosity, surface boundary conditions, and bottom drags) based on a Green's function approach (Menemenlis et al., 2005), the ECCO2 model is run unconstrained as in prognostic model simulations. As no observational data are imposed in the forward integration, the ECCO2 output can be considered as dynamically and thermodynamically consistent (Wunsch et al., 2009). This point is important to our study as the water mass property changes associated with the CS intraseasonal eddy variability are

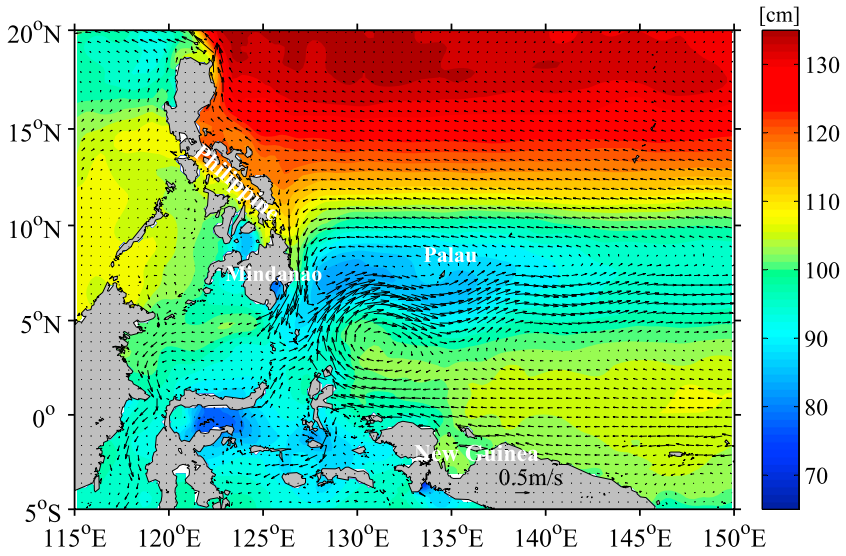

Figure 1. Mean sea surface height (colors) in the western Pacific based on satellite altimetry observations. The black arrows indicate the mean surface currents from the Estimating the Circulation and Climate of the Ocean, Phase II state estimate. Both results are averaged from 1993 to 2016.

dynamically and thermodynamically constrained consistently in the ECCO2 product. The ECCO2 state estimate has been used in the past to examine the eddy variability in different parts of the global ocean (e.g., Chen et al., 2014; Fu, 2009; Qiu et al., 2017; Zemskova et al., 2015). For this study, we use the 3-day averaged ECCO2 output from 1993 to 2016 (http://apdrc.soest.hawaii.edu/datadoc/ecco2_cube92.php).

To verify aspects of the ECCO2 state estimate in the region of our interest, we use in this study the merged SSH anomaly data distributed by Archiving, Validation, and Interpolation of Satellite Oceanographic (AVISO) data (http://www.aviso.oceanobs.com/) that combines simultaneous measurements from two satellite altimeters (TOPEX/Poseidon or Jason-1 and ERS or Envisat). The AVISO SSH data have a 1/3° × 1/3° horizontal resolution and a 7-day temporal resolution. To synchronize with the time period of the ECCO2 output, the AVISO SSH data from 1993 to 2016 are used for this study.

3. Verification of ECCO2 State Estimate

Although the 50-day oscillation is a localized phenomenon inside the CS, its interannual modulation can be expected to be controlled by broadscale conditions in the tropical western Pacific Ocean. As such, before exploring the dynamical processes governing the interannual modulations of eddy variability inside the CS, it is important to verify the broadscale oceanic variability surrounding the CS in the ECCO2 state estimate against the available satellite altimetry measurements. Figure 1 compares the 1993–2016 time-mean surface circulation distributions in the tropical western Pacific Ocean: The vectors show the surface velocity field from the ECCO2 output, and the colored contours represent the AVISO SSH field. The two fields correspond favorably through the geostrophic balance, including the bifurcation of the westward-flowing North Equatorial Current at ~12.5°N along the Philippine coast, the southward-flowing Mindanao Current's splitting into the westward-flowing ITF in the CS, and the retroflecting, eastward-flowing North Equatorial Countercurrent (NECC). Continuation of the ITF entering the Makassar Strait and retroflection of the New Guinea Coastal Current from south of the equator to merge with the Mindanao Current and form the NECC are both discernible in Figure 1.

To compare the time-varying signals between the ECCO2 and AVISO data sets, we conduct an empirical orthogonal function (EOF) analysis to the ECCO2 and AVISO SSH anomaly data in 1993–2016. Figures 2a and 2c show the spatial pattern of EOF mode 1 from the ECCO2 and AVISO analysis, respectively. This mode explains 63.4% and 55.1% of the total SSH variance in the ECCO2 and AVISO data, respectively. The two spatial patterns reveal good resemblance not only in the open western Pacific Ocean but also in marginal seas

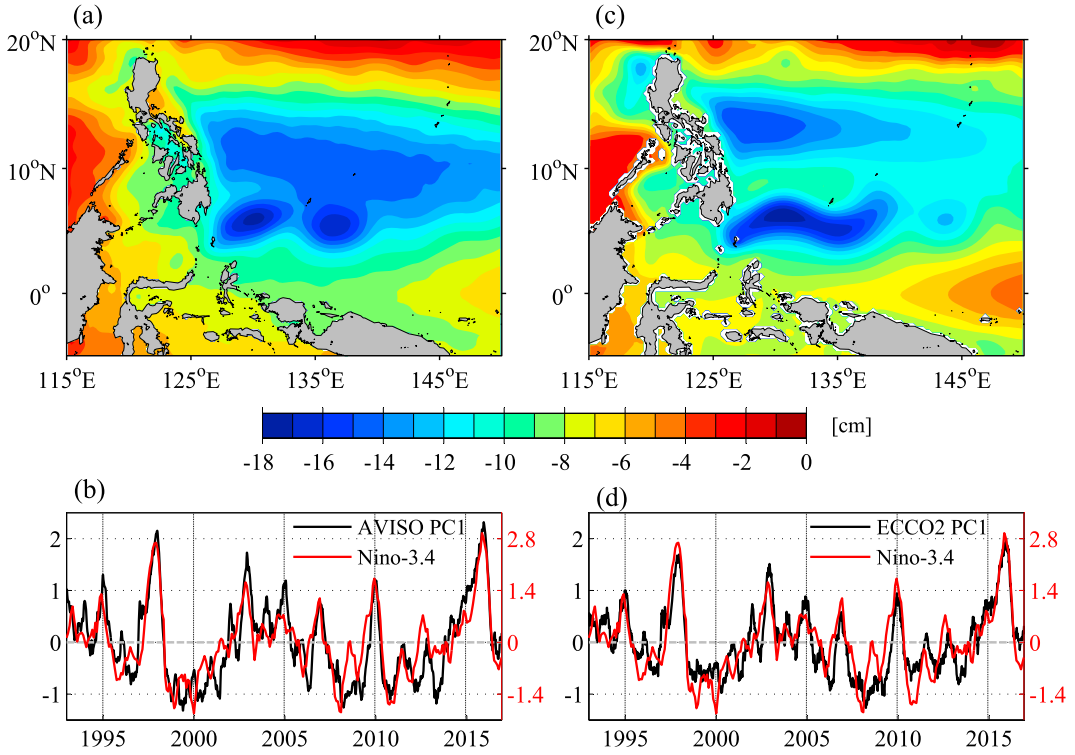

Figure 2. (a, b) Spatial pattern and principal component (PC) of empirical orthogonal function mode 1 of sea surface height anomalies from the Archiving, Validation, and Interpolation of Satellite Oceanographic (AVISO) data set. (c, d) Same as (a, b) except from the Estimating the Circulation and Climate of the Ocean, Phase II (ECCO2) simulation. Red lines in (b) and (d) indicate Niño-3.4 index.

inside the Makassar Strait, the CS, the Sulu Sea, and the eastern South China Sea. A zonal SSH ridge along ~9°N appears, however, more pronounced in the ECCO2 EOF result than AVISO data. The spatial correlation coefficient between Figures 2a and 2c is $r = 0.87$. The principal component (PC) time series of the EOF mode 1s are shown in Figures 2b and 2d, respectively. Like their spatial patterns, the two PC time series, shown by the dark black lines in Figures 2b and 2d, also match very favorably with a linear correlation coefficient reaching $r = 0.96$. Temporally, the EOF mode-1 PC time series exhibit close connections to the Niño-3.4 index shown by the red lines: The highest linear correlation coefficient is found at $r = 0.82$ and 0.80 in Figures 2b and 2d, respectively, when the Niño-3.4 index lags the two PC time series by 1 month. Physically, the EOF mode 1 represents the large-scale SSH changes in the tropical western Pacific Ocean in response to the dominant ENSO-modulated wind forcing. Specifically, during the mature phase of El Niño events, the western Pacific SSH anomaly tends to have a high-low-high tripolar meridional structure, reflecting the intensification and northward expansion of the NECC and North Equatorial Current (e.g., Chen et al., 2016; Qiu & Lukas, 1996; Zhao et al., 2013). From Figure 2, it is clear that the ECCO2 state estimate captures faithfully the observed ENSO-induced large-scale circulation variability in the tropical western Pacific Ocean.

To some degree, it may not be surprising that the dominant ENSO-induced variability is fully captured by ECCO2. However, it is encouraging to see that the ECCO2 state estimate is capable to simulate the EOF mode 2 of the AVISO SSH signals equally well, both in terms of their spatial patterns (Figures 3a and 3c) and their PC time series (Figures 3b and 3d). The correlation coefficient between the spatial patterns is $r = 0.89$ and that between the PC time series is $r = 0.94$. As can be identified in the PC time series, the EOF mode 2 represents the seasonal SSH changes that modulate interannually in the tropical western Pacific Ocean. Unlike mode 1, the EOF mode-2 SSH pattern has a dipolar meridional structure and it reflects the meridional shift of the NECC on the seasonal time scale. Consistent with the previous data analyses by Hsin and Qiu (2012) and Zhao et al. (2013), Figure 3 indicates the NECC is stronger and more northerly in winter and weaker and more southerly in summer. Although the variance explained by the EOF mode 2 is relatively low (16.5% in the ECCO2 output

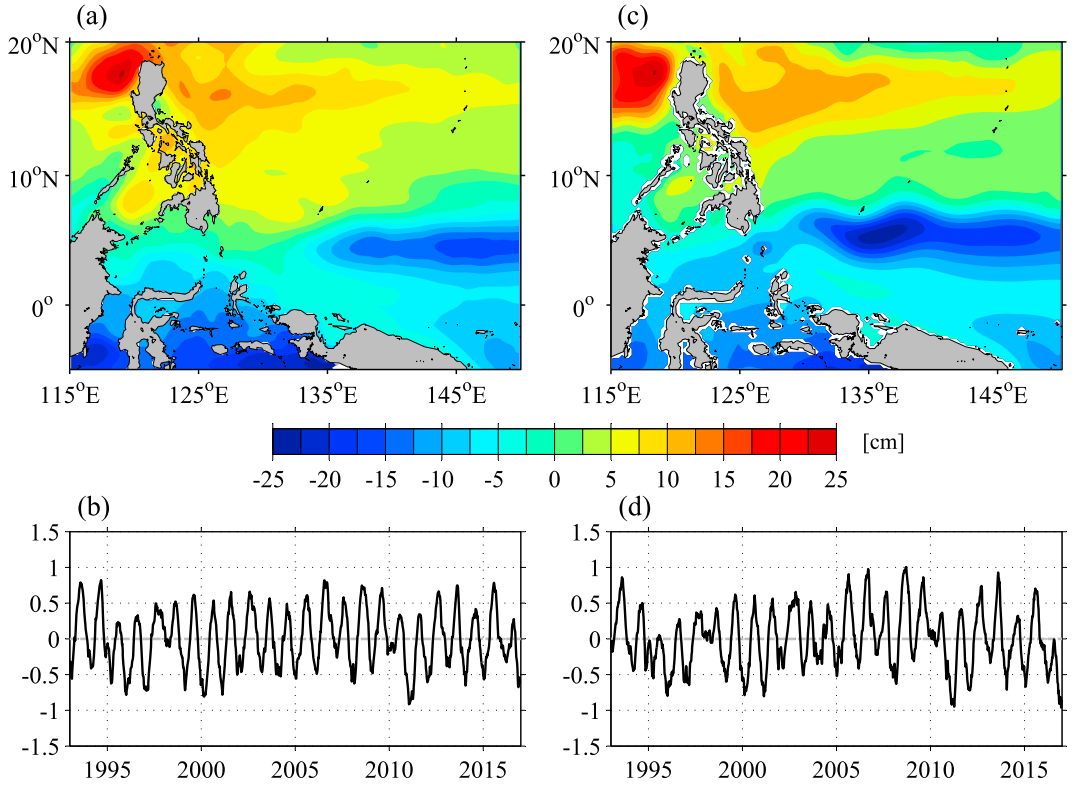

Figure 3. (a, b) Spatial pattern and principal component of empirical orthogonal function mode 2 of sea surface height anomalies from the Archiving, Validation, and Interpolation of Satellite Oceanographic data set. (c, d) Same as (a, b) except from the Estimating the Circulation and Climate of the Ocean, Phase II simulation.

and 16.3% in the AVISO data), the interannual signals of this mode, as we will uncover in section 5, are closely related to the interannual modulations of the intraseasonal signals inside the CS.

The fact that the ECCO2 state estimate is able to successfully simulate the leading two EOF mode signals observed in the tropical western Pacific Ocean is important because these large-scale low-frequency circulation changes are dynamically responsible for the interannual modulations in the surrounding marginal sea circulation, including that in the CS of our interest. Because of the tidal aliasing issue noted in section 1, we will explore in this study the 50-day oscillation and its interannual modulations in the CS based on the 3-day ECCO2 output only.

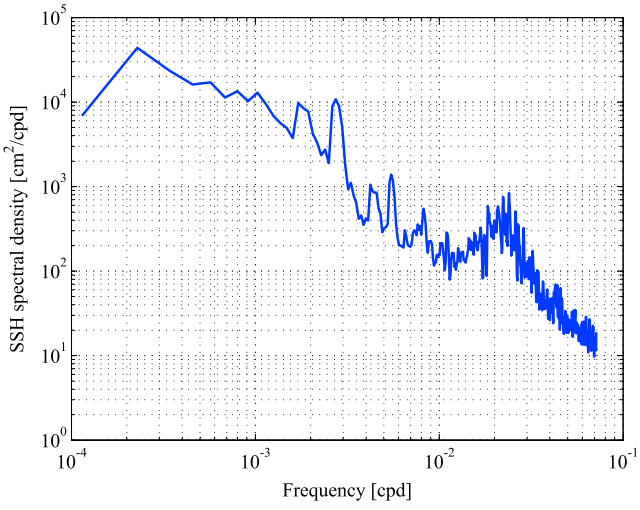

Figure 4. Frequency spectrum of sea surface height variance averaged in the box of 1°N–6°N, 117°E–125°E inside the Celebes Sea.

4. Fifty-Day Oscillation and Its Interannual Modulations

To quantify the frequency content of the time variability inside the CS, we plot in Figure 4 the power spectrum of the ECCO2 SSH data in the area 117°E–125°E and 1°N–6°N of the CS basin. Aside from the localized spectral peaks at the annual and semiannual frequencies (2.73×10^{-3} and 5.48×10^{-3} cpd), there exists enhanced SSH variability in the intraseasonal band of 40–60 days (frequency = $1.6–2.5 \times 10^{-2}$ cpd) in accordance with the observational findings by Kashino et al. (1999) and Napitu et al. (2015). To confirm these 40- to 60-day SSH variability in the physical space, we show in Figure 5 the time-longitude diagram of the 100-day high-pass filtered SSH anomalies along 4°N, the center latitude of the CS. For high-pass filtering, we utilize the MATLAB built-in function filtfilt (b,a,input-timeseries), where [b,a] = butter (10,1/(100/3)*2,'high'). The

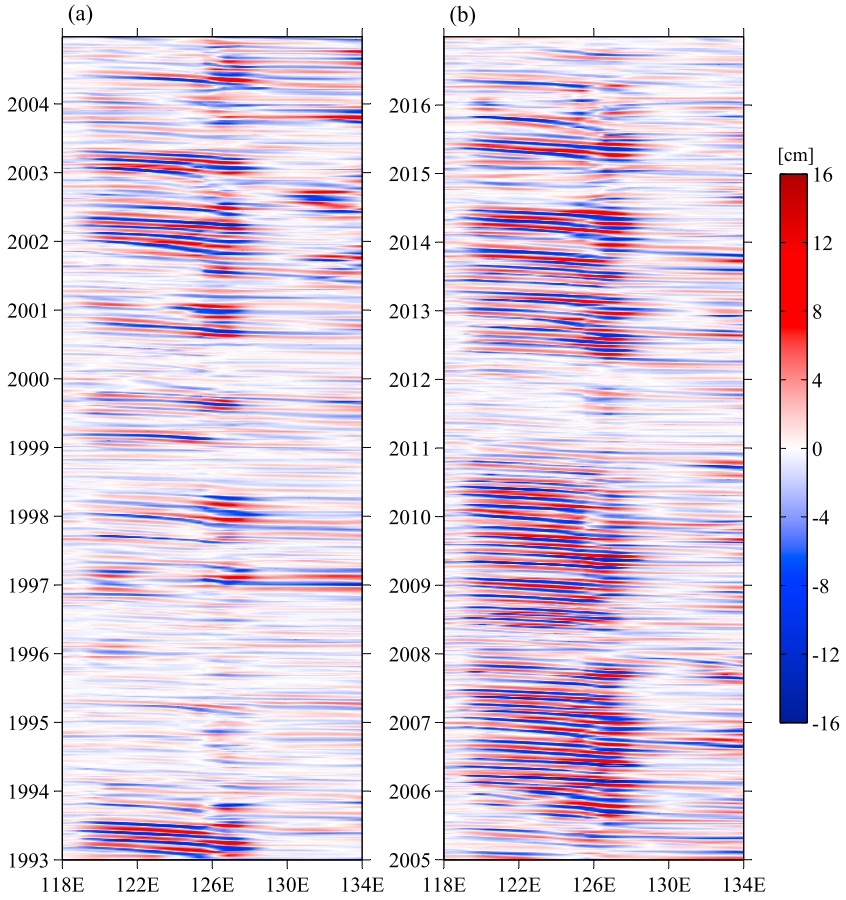

Figure 5. Time-longitude diagram of 100-day high-pass filtered sea surface height anomalies along 4°N. The Celebes Sea entrance is located approximately at 126°E.

longitude range in Figure 5 covers from 118°E to 134°E. With the CS eastern boundary located near 126°E, Figure 5 reveals that the intraseasonal variability inside the CS basin of 118°E–126°E is distinct from that in the open Pacific Ocean east of 128°E. Inside the CS basin, the intraseasonal eddy signals show zonally coherent westward propagation with a speed at 0.12 m/s and the dominance of the 40- to 60-day oscillation is clearly identifiable. To visualize the life cycle of the 40- to 60-day oscillation signals captured in Figure 5, it is instructive to examine a representative event that occurred between 8 November 2009 and 12 February 2010. As shown in Figures 6a–6c, the retroflecting Mindanao Current south of the Mindanao Island formed a cyclonic eddy that grew progressively during November and early December in 2009. On 14 December, this cyclonic eddy pinched off from the retroflecting Mindanao Current (Figure 6d) and increased in amplitude while propagating westward at a speed of 0.12 m/s (Figures 6e and 6f). After reaching the CS western boundary, the cyclonic eddy weakened and moved subsequently southward (Figures 6g and 6h). By 12 February 2010 (Figure 6i), the cyclonic eddy was largely dissipated and only a weak remnant of it can be discerned at the northern entrance near 1°N of the Makassar Strait. Notice that in Figure 6h, about 60 days after the initial cyclonic eddy pinched off from the Mindanao Current, a second cyclonic eddy can be seen to start to pinch off at the same location from the retroflecting Mindanao Current at south of the Mindanao Island.

From Figure 5, it is clear that the intensity of the 40- to 60-day oscillation inside the CS changes from year to year. To emphasize this point, we plot by the red lines in Figure 7 the EKE time series inside the CS basin (117°E–125°E, 1°N–6°N) based on the surface velocity data that is high-pass filtered at 100 days. Consistent with Figure 5, it reveals significant kinetic energy level fluctuations on the interannual time scales. In order to better quantify the interannual modulations of the intraseasonal eddy variability inside the CS, we

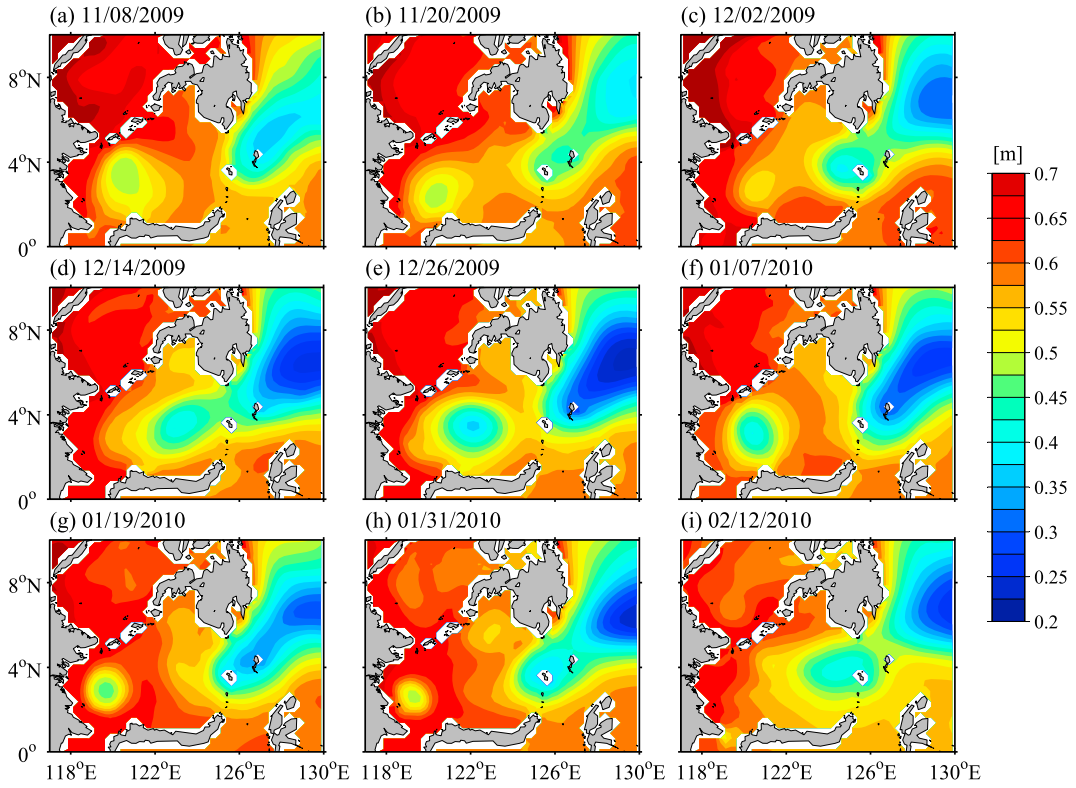

Figure 6. Sequential maps of sea surface height field from 8 November 2009 to 12 February 2010. Interval between each map is 12 days.

introduce in this study the 50-day oscillation index, I_{50d}, defined by low-pass filtering the intraseasonal kinetic energy time series shown in Figure 7 to remove the signals shorter than 1.5 years. For low-pass filtering, we utilize the MATLAB built-in function filtfilt (b,a,input-timeseries), where [b,a] = butter (6,1/(548/3)*2,'low'). The I_{50d} is shown in Figure 7 by the thick black line. According to this definition, high I_{50d}, or active 40- to 60-day oscillation, years are seen in 1993, 2002–2003, 2006–2010, and 2012–2015.

5. Mechanisms Behind Interannual Modulations

To clarify the dynamical processes behind the interannual modulations of 40- to 60-day oscillations inside the CS, we regress the ECCO2 SSH and surface velocity anomaly fields to the 50-day oscillation index I_{50d} (see Figures 8a and 8b). In the regressed SSH field, Figure 8a reveals a dipolar meridional pattern quite similar to that of the EOF mode 2 (recall Figure 3c), with the dipole boundary aligned roughly along 8°N. Relative

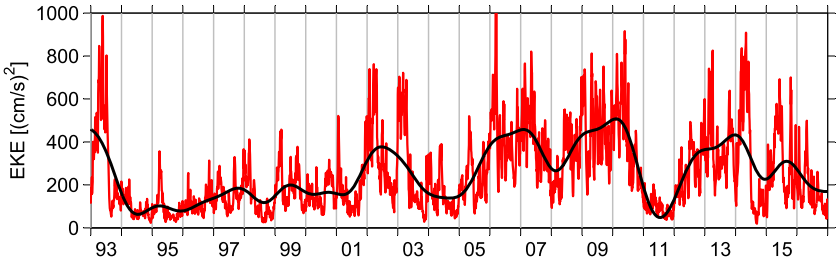

Figure 7. Eddy kinetic energy (EKE) time series (red line) averaged in the Celebes Sea basin of 117°E–125°E and 1°N–6°N based on Estimating the Circulation and Climate of the Ocean, Phase II 100-day high-pass filtered surface velocity data. The black line denotes the 1.5-year low-pass filtered EKE time series and is defined as the 50-day oscillation index, I_{50d}, in this study.

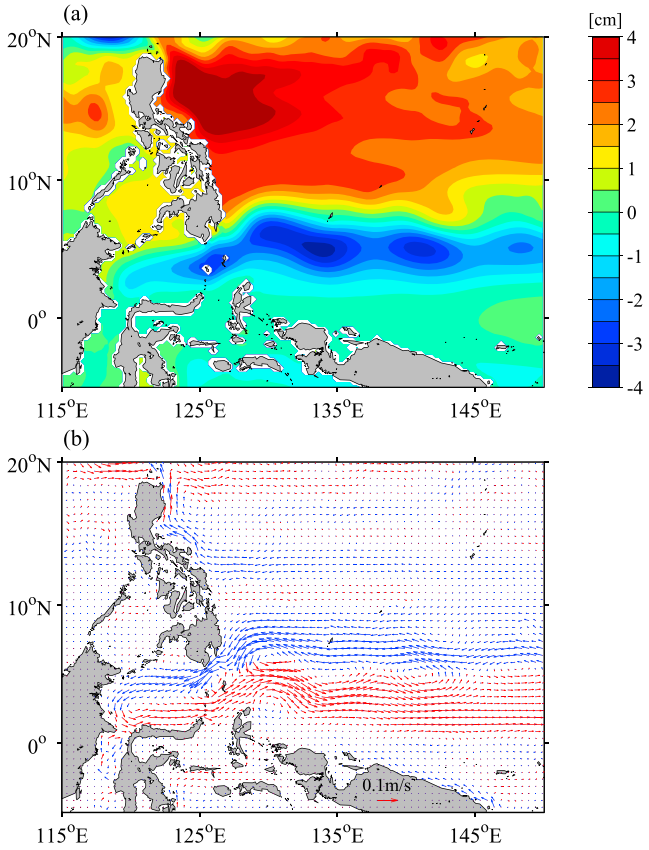

Figure 8. Regressed (a) sea surface height and (b) surface velocity field to the 50-day oscillation index, I_{50d}. Velocity vectors with positive (negative) u component are indicated in red (blue).

to the time-mean surface velocity field shown in Figure 1, the regressed velocity field in Figure 8b suggests a southward migration of the wind-driven tropical gyre, an intensification of the Mindanao Current southeast of the Mindanao Island and its westward intrusion into the CS, and an increased southward flow of the ITF during the high I_{50d} years.

It is worth noting that the 50-day oscillation index corresponds well to the interannual signals captured in the EOF mode-2 PC time series of Figure 3d. As shown in Figure 9, the time series of the low-pass filtered PC 2 and I_{50d} have a linear correlation coefficient reaching 0.72. Dynamically, this good correlation implies that instead of a regional phenomenon, the interannual modulations in the 40- to 60-day oscillations inside the CS have an origin in the broader tropical Pacific Ocean.

Since our defined 50-day oscillation index reflects the dipolar SSH changes across 8°N (Figure 8a), it is of interest to relate I_{50d} to the SSH anomaly signals in the tropical western Pacific Ocean. To do so, we plot in Figures 10a and 10b (solid lines) the low-pass filtered SSH anomaly time series $h_N(t)$ and $h_S(t)$ in the box (128°E–145°E, 8°N–12°N) and (128°E–145°E, 3°N–7°N) north and south of the dipolar SSH boundary, respectively. Not surprisingly, the SSH difference, $h_N(t) - h_S(t)$, time series shown in Figure 10c by the solid line compares favorably with the I_{50d} time series (the dashed line in Figure 10c). The two time series in Figure 10c have a linear correlation coefficient at $r = 0.76$. This high correlation suggests that examining the 50-day oscillation index is equivalent to examining the time-varying SSH anomalies of $h_N(t)$ and $h_S(t)$ in the tropical western Pacific Ocean.

In the tropical Pacific Ocean, large-scale SSH variability is induced predominantly by the time-varying surface wind forcing (see Qiu & Chen, 2010, and references therein). Under the long-wave approximation, the linear vorticity equation governing the SSH anomaly $h(x,y,t)$ in the 1.5-layer reduced-gravity model is given by

$$\frac{\partial h}{\partial t} - C_R \frac{\partial h}{\partial x} = -\frac{g'}{g\rho_0} \nabla \times \left(\frac{\vec{\tau}}{f} \right) - \varepsilon h, \tag{2}$$

where $C_R(x,y)$ is the phase speed of long baroclinic Rossby waves, g' is the reduced gravity, ρ_0 is the reference density, $\vec{\tau}$ is the surface wind stress anomaly vector, and ε is the Newtonian dissipation rate. Integrating equation (2) from the eastern boundary ($x = x_e$) along the characteristic of baroclinic Rossby waves (constant y in the present case), we can solve $h(x,y,t)$ by

$$h(x,y,t) = \frac{g'}{g\rho_0} \int_{x_e}^{x} \frac{1}{C_R} \nabla \times \left[\vec{\tau}\left(x', y, t + \frac{x - x'}{C_R} \right) / f \right] \times \exp\left[\frac{\varepsilon}{C_R} (x - x') \right] dx'. \tag{3}$$

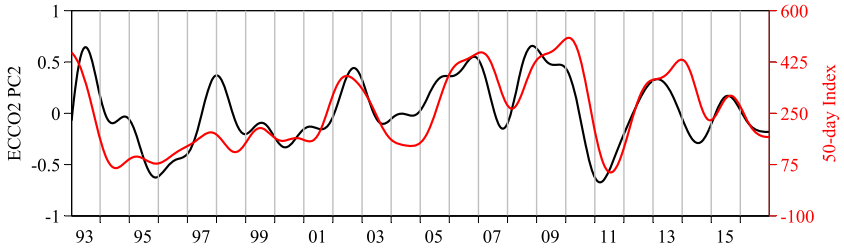

Figure 9. Comparison between the Celebes Sea 50-day oscillation index (red line) and the 1.5-year low-pass filter principal component (PC) of empirical orthogonal function mode 2 of sea surface height anomalies from the Estimating the Circulation and Climate of the Ocean, Phase II (ECCO2) product (black line).

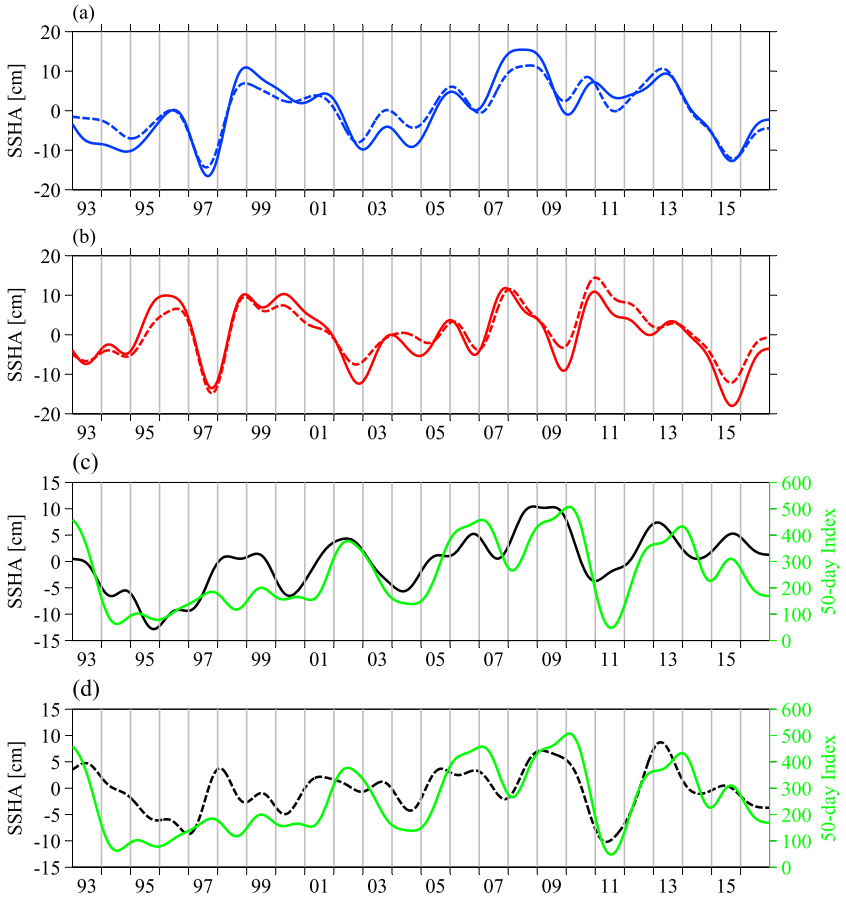

Figure 10. Time series of sea surface height anomalies (SSHAs) averaged in box (a) 128°E–145°E, 8°N–12°N and (b) 128°E–145°E, 3°N–7°N. Solid lines denote the time series from Estimating the Circulation and Climate of the Ocean, Phase II state estimate and dashed lines, those from the wind-forced linear vorticity model. All time series are after a 1.5-year low-pass filtering. Black line in (c) denotes the SSHA difference between the solid lines in (a) and (b), and green line shows the 50-day oscillation index, I_{50d}. (d) Same as (c) except the dashed black line denotes the SSHA difference between the dashed lines in (a) and (b).

In the above solution, we have ignored the signal of SSH anomalies at the eastern boundary as its effect has been shown to have little impact on the SSH variability in the western Pacific (Fu & Qiu, 2002). To evaluate equation (3), we use $g' = 0.04$ m/s^2, $\varepsilon^{-1} = 1.6$ year, and the monthly wind stress data from the European Centre for Medium-Range Weather Forecasts Interim Re-Analysis (ERA-Interim) product that has a spatial resolution of 0.75° × 0.75°(Dee et al., 2011). Notice that the ERA-interim wind stress data were used as an external forcing for the ECCO2 state estimate. Although these wind stress data are adjusted as a result of assimilation, their adjustment is quite minor across the tropical North Pacific basin of our interest (figure not shown). The wind-forced model results shown below are insensitive to whether we use the original or ECCO2-adjusted wind stress data in equation (3).

The dashed lines in Figures 10a and 10b show the time series of $h_N(t)$ and $h_S(t)$ in the two tropical western Pacific boxes based on equation (3). Despite its simplicity, the wind-forced linear vorticity model is able to reproduce the ECCO2 h_N and h_S time series very favorably: The correlation coefficient between the solid and dashed lines in Figure 10a (Figure 10b) is as high as 0.94 (0.93). Use of equation (3) further allows us to quantify the relative contributions of wind forcing across different parts of the Pacific basin that is responsible for the $h_N(t)$ and $h_S(t)$ changes. To pursue this, it is useful to define

$$\overline{h}(X,t) = \frac{g'}{\rho_o g L_x L_y}\int_{y_S}^{y_N}\int_{128^\circ\mathrm{E}}^{145^\circ\mathrm{E}}\left\{\int_X^x \frac{1}{C_R}\nabla\times\left[\vec{\tau}\left(x',y,t+\frac{x-x'}{C_R}\right)/f\right]\exp\frac{\varepsilon(x-x')}{C_R}dx'\right\}dxdy, \quad (4)$$

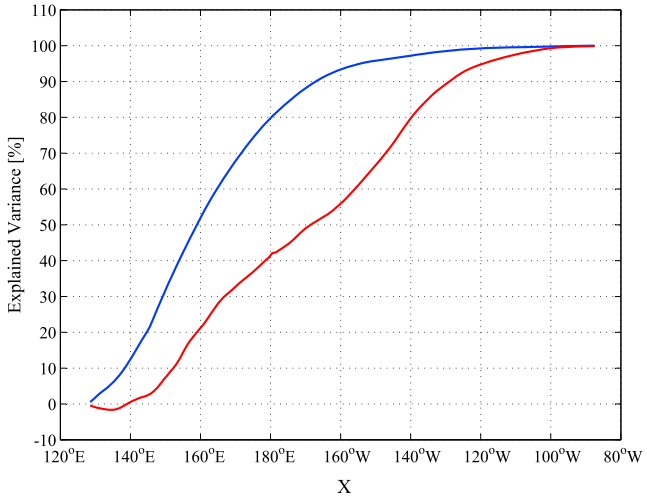

Figure 11. Explained percent of variance of sea surface height anomalies in the northern box (blue) versus the southern box (red) by the accumulative wind forcing from 128°E to longitude *X*. See equation (4) and the text for details.

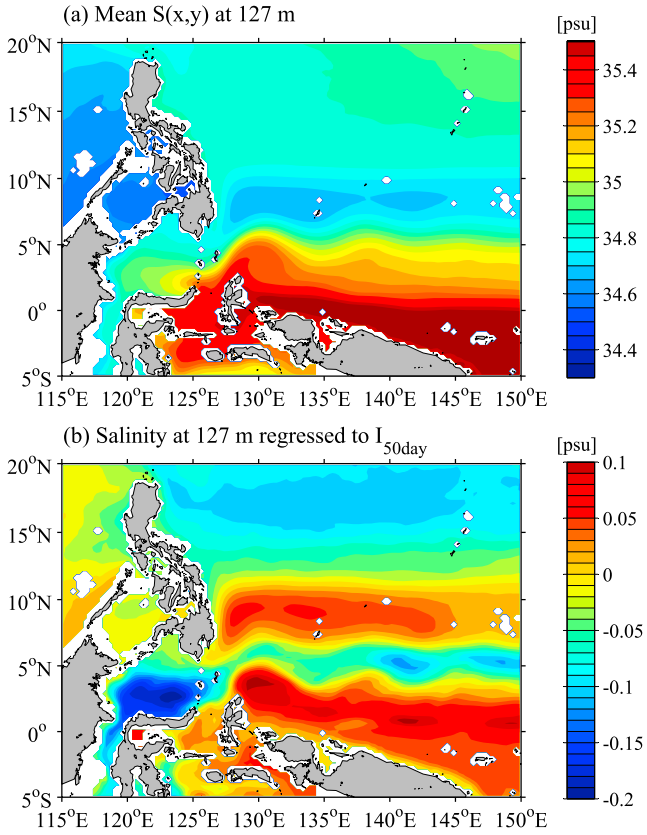

Figure 12. (a) Mean salinity distribution at the 127-m depth from the 1993–2016 Estimating the Circulation and Climate of the Ocean, Phase II product. (b) Salinity anomaly distribution regressed to the 50-day oscillation index I_{50d}.

where (y_S, y_N) = (3°N, 7°N) for the southern box and (8°N, 12°N) for the northern box and L_xL_y denotes the area of these boxes. Physically, $\overline{h}(X,t)$ indicates the box-averaged SSH anomalies induced by the wind forcing that exists west of longitude *X*. By definition, $\overline{h}(x_e,t)$ gives the time series forced by the basin-wide wind forcing and is shown by the dashed line in either Figure 10a or Figure 10b.

The red (blue) line in Figure 11 shows the variance of the $\overline{h}(x_e,t)$ time series in the southern (northern) box explained by the wind forcing west of *X* as a function of latitude:

$$S(X) \equiv 1 - \frac{\left\langle \left[\overline{h}(x_e,t) - \overline{h}(X,t)\right]^2 \right\rangle}{\left\langle \overline{h}^2(x_e,t) \right\rangle}, \tag{5}$$

where $\langle\rangle$ denotes the ensemble average in time. Comparing the two lines reveals that the wind forcing in the western Pacific plays a more dominant role in changing the northern-box SSH signals than those in the southern box. Specifically, the wind forcing west of the dateline alone can explain 80% of the $h_N(t)$ variance. To account for the same amount of the $h_S(t)$ variance, wind forcing over the wider range of 128°E–140°W is required.

Similar to the ECCO2 result shown in Figure 10c, the $h_N(t) - h_S(t)$ time series based on equation (3) exhibits a good correlation to the I_{50d} time series. The linear correlation coefficient between the black and green lines in Figure 10d reaches $r = 0.72$, comparable to the $r = 0.76$ value obtained in Figure 10c. The results in Figures 10 and 11 confirm that it is the cumulative effect of wind forcing across the tropical Pacific basin that controls the interannual modulations of the intraseasonal eddy variability inside the CS.

6. Impact of Interannually Modulating 50-Day Oscillations

As we noted in Introduction, the CS is the basin where Southern and Northern Hemispheres-origin waters intermingle and it is this admixture of waters that comprises the water mass of the originating ITF. To demonstrate this point visually, we plot in Figure 12a the salinity distribution at the 127-m depth averaged from the ECCO2 output of 1993–2016. The CS salinity value around 35.0 psu falls clearly in between the saline South Pacific water with $S > 35.4$ psu and the fresh North Pacific water with $S < 34.6$ psu. To assess the impact of the 40- to 60-day eddy variability upon the salinity signals inside the CS and its downstream Makassar Strait, we plot in Figure 12b the time-varying salinity signals regressed to the I_{50d} time series. Inside the CS basin and the Makassar Strait, there exists a clear negative value, indicating that as the level of 40- to 60-day eddy activity increases, more North Pacific-origin fresh water tends to penetrate into the CS and its downstream region. Physically, this is consistent with the eddy evolution pattern depicted in Figure 6: The 40- to 60-day eddies that penetrate into the CS have their North Pacific origin in the Mindanao Current and an enhanced eddy activity can be expected to lower the CS salt content through lateral salt transport.

To examine the effect of the 40- to 60-day oscillation signals upon the water masses more quantitatively, we plot in Figure 13a the vertical salinity profile as a function of time at a center location (122°E–123°E, 3°N–

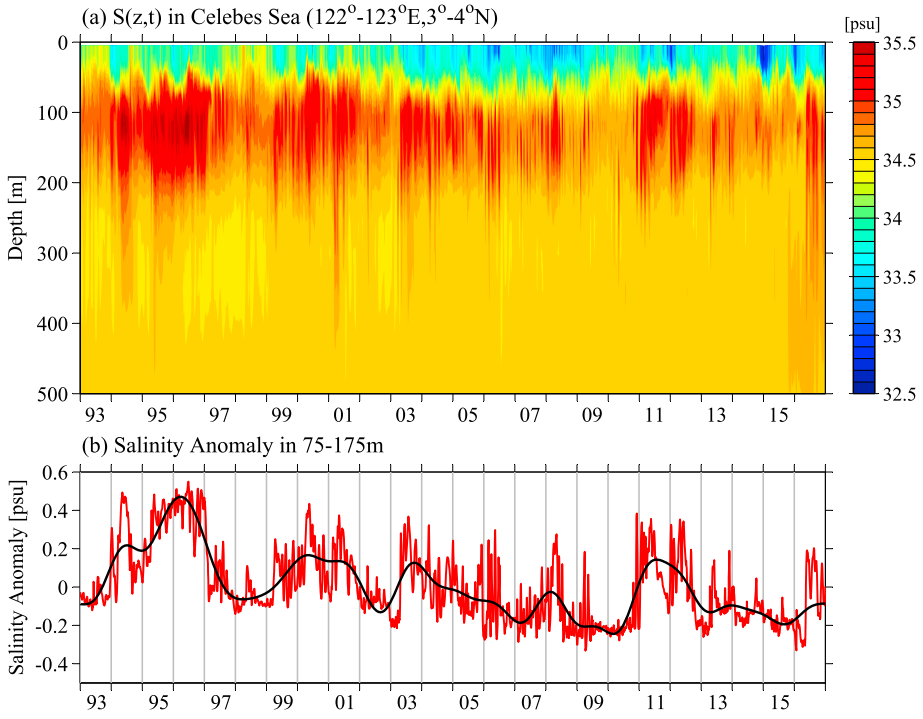

Figure 13. (a) Time-varying salinity profile averaged in the Celebes Sea box 122°E–123°E and 3°N–4°N. (b) Salinity anomaly time series in the 75- to 175-m layer (red line). Black line shows the interannual signals after a 1.5-year low-pass filtering.

4°N) inside the CS. A particular feature of our interest is the salinity maximum water that exists in the 75- to 175-m depth, known as the Tropical Water (e.g., Fine et al., 1994). Figure 13b shows the salinity anomaly time series at this location averaged in the 75- to 175-m layer. Consistent with the regression result shown in Figure 12b, the low-frequency salinity variability shown by the black line in Figure 13b exhibits a negative

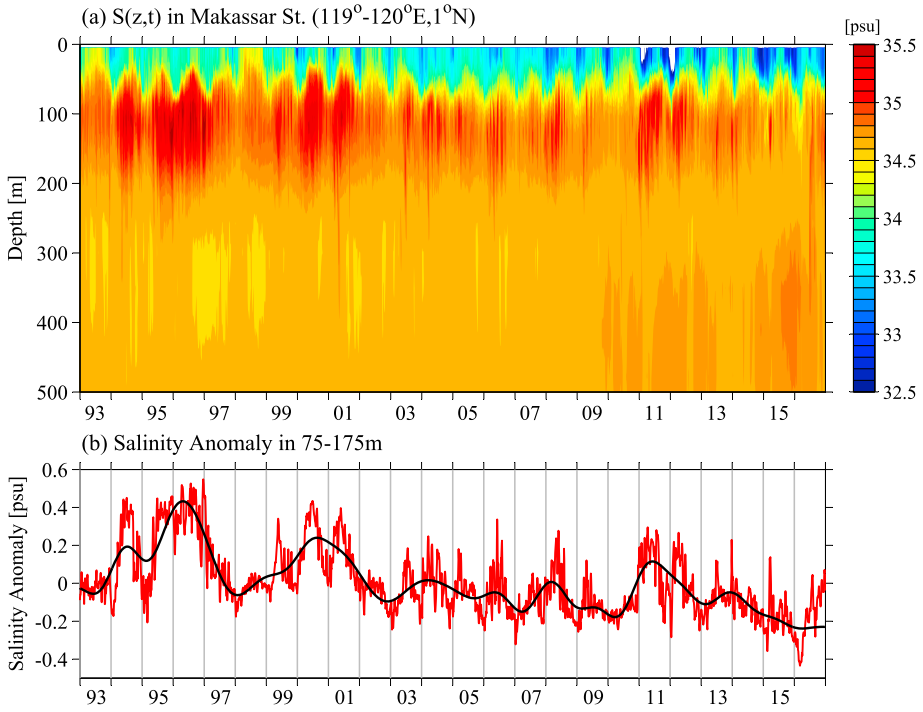

Figure 14. Same as Figure 13 except for the salinity signals in the Makassar Strait entrance of 119°E–120°E and 1°N.

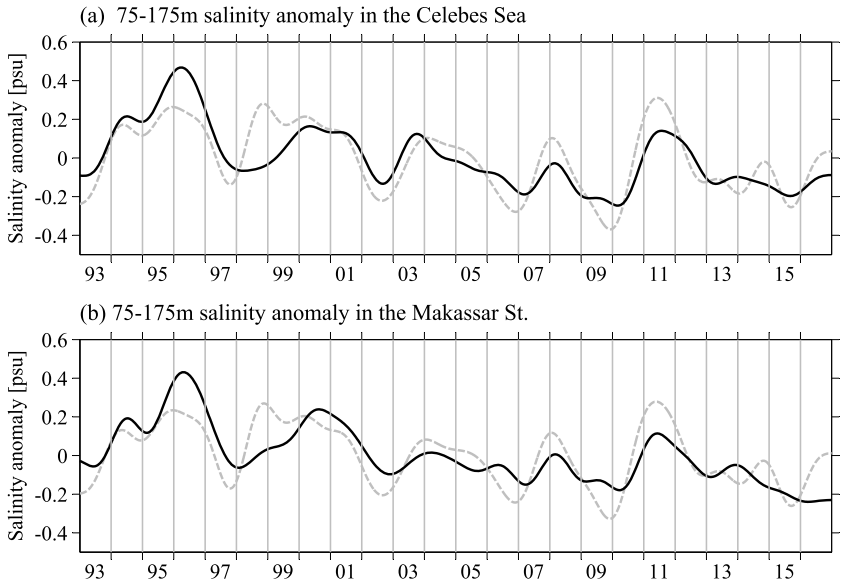

Figure 15. Black lines: Salinity anomaly time series in (a) the Celebes Sea and (b) the Makassar Strait entrance (same as the black lines in Figures 13b and 14b). Dashed lines: Best-fit $\alpha I'_{50d}(t) + \beta N'(t)$ time series based on equation (4).

correlation, $r = -0.77$, with the I_{50d} time series. When I_{50d} is high in 1993, 2002, 2006–2010, and 2013–2015, for example, the salinity anomaly values are generally low. The long-term freshening trend seen in Figure 13b is also consistent with the overall increasing trend in I_{50d}. A very similar salinity variability is detected in the 75- to 175-m layer at the entrance of the Makassar Strait at 119°E–120°E and 1°N (Figure 14). Compared to Figure 13b, the salinity anomalies associated with the salinity-maximum Tropical Water at the Makassar Strait tend to have smaller amplitude and their correlation with the I_{50d} time series is also lower at $r = -0.65$.

Given the modest correlation between the salinity anomaly signals and I_{50d} in Figure 14b, it is relevant to explore other dynamical processes that could contribute to the salinity changes inside the Makassar Strait. One obvious candidate for such process is the El Niño–Southern Oscillation (ENSO) variability in the western tropical Pacific Ocean as captured by the mode-1 EOF of the SSH field shown in Figure 2. To quantify the relative contributions to the salinity changes from the 40- to 60-day eddy modulations and the ENSO variability, we conduct a multiple linear regression analysis (Emery & Thomson, 2001) by assuming

$$S'(t) = \alpha I'_{50d}(t) + \beta N'(t) + \varepsilon, \tag{6}$$

where $S'(t)$ is the low-frequency salinity signals of our interest shown by the black line in either Figure 13b or Figure 14b, $I'_{50d}(t)$ is the normalized I_{50d} index, $N'(t)$ is the normalized low-pass filtered Niño-3.4 index, and ε is the residual error. By determining α and β through least squares fitting, equation (6) allows us to evaluate the correlation between $S'(t)$ and the combined effect of 40- to 60-day eddy modulations and ENSO variability, namely, $\alpha I'_{50d}(t) + \beta N'(t)$.

Figure 15a compares $S'(t)$ and the best-fit $\alpha I'_{50d}(t) + \beta N'(t)$ for the CS salinity signals. Compared to the correlation coefficient $|r| = 0.77$ between $S'(t)$ and $I'_{50d}(t)$, adding the contribution from the ENSO variability increases the correlation coefficient to $r = 0.79$ only. In comparison to the CS case, the change in r value in the Makassar Strait case by adding the ENSO-induced variability is more substantial: While $|r| = 0.65$ between $S'(t)$ and $I'_{50d}(t)$, the correlation between $S'(t)$ and $\alpha I'_{50d}(t) + \beta N'(t)$ increases to $r = 0.74$ or a 14% improvement (Figure 15b). These results from the multiple regression analysis indicate that while the 40- to 60-day eddy modulations dictate the variability of the salinity maximum water inside the CS, their impact becomes weaker in the downstream Makassar Strait, where the salinity maximum water is affected additionally by the low-frequency ENSO modulations.

7. Summary

CS is an important gateway that connects the Pacific and Indian Oceans. Due to its basin geometry, the CS is subject to resonant amplification of 40- to 60-day oscillations. Using the ECCO2 ocean state estimate product of 1993–2016, we found that the 40- to 60-day oscillations inside the CS underwent intense interannual modulations. Compared to a basin-averaged EKE level of less than 0.02 m^2/s^2 in weak oscillation years, the active oscillation years in 1993, 2002–2003, 2006–2010, and 2013–2015 had an EKE level exceeding 0.04 m^2/s^2.

The interannual modulations of the CS 40- to 60-day oscillations are related to the second-mode EOF of the interannually varying SSH field in the western tropical Pacific Ocean. Specifically, active 40- to 60-day oscillations occur when the wind-driven tropical/subtropical gyres migrate equatorward and the Mindanao Current to the southeast of the Mindanao Island intensifies. Dynamically, the interannual modulation amplitude of the 40- to 60-day oscillations is represented well by the sea level difference signals in the western tropical Pacific Ocean (128°E–145°E) north and south of 7.5°N. Instead of the regional monsoonal wind forcing, quantification using a linear vorticity model reveals that it is the basin-wide wind forcing extending at least to 140°W that determines the 40- to 60-day oscillation modulations via baroclinic Rossby wave adjustment.

An examination of water mass property changes indicates that the 40- to 60-day oscillation modulations affect the salinity-maximum Tropical Water inside the CS and Makassar Strait. During the active years of 40- to 60-day oscillations, increased eddy activities work to transport fresher North Pacific-origin water into the CS, resulting in lowered salt content in the salinity-maximum Tropical Water. In addition to the 40- to 60-day oscillations, the low-frequency salinity variability in the Makassar Strait is also subject to the ENSO-modulated circulation changes. The result that the 40- to 60-day oscillation effect weakens in the downstream Makassar Strait is likely related to the dissipation of 40- to 60-day eddies when they reach the western boundary of the CS and have to squeeze into the narrow Makassar Strait (recall Figure 6). Despite this weakening, an analysis of the mooring observations across the Labani Channel by Pujiana et al. (2012) suggested that the CS 40- to 60-day fluctuations are able to affect the across-channel flow near 3°S in the Makassar Strait. At present, the processes by which the 40- to 60-day eddies interact with the CS western boundary and transform within the narrowed Makassar Strait are not well understood. Clearly, future studies are needed to clarify these processes for a better understanding about the ITF impact by the 40- to 60-day oscillations initiated in the CS.

Acknowledgments
We thank the two reviewers for their detailed and constructive comments that helped improve an early version of the paper. The ECCO2 state estimate data set is available at http://apdrc.soest.hawaii.edu/datadoc/ecco2_cube92.php, the AVISO SSH data at http://www.aviso.oceanobs.com/, and the ERA-Interim wind stress data at http://apdrc.soest.hawaii.edu/datadoc/ecmwf_era-interim.php. This study is supported by the National Natural Science Foundation of China (grant 41706004), the Natural Science Foundation of Jiangsu Province (grant BK20170872), the Fundamental Research Funds for the Central Universities (grants 2017B04614 and 2017B04114), the National Natural Science Foundation of China (grants 41522601 and 41776004), the Natural Science Foundation of Jiangsu Province (grant BK20170870).

References

Broecker, W. S. (1991). The great ocean conveyor. *Oceanography*, *4*(2), 79–89. https://doi.org/10.5670/oceanog.1991.07

Chen, R., Flierl, G. R., & Wunsch, C. (2014). A description of local and nonlocal eddy-mean flow interaction in a global eddy-permitting state estimate. *Journal of Physical Oceanography*, *44*(9), 2336–2352. https://doi.org/10.1175/JPO-D-14-0009.1

Chen, X., Qiu, B., Du, Y., Chen, S., & Qi, Y. (2016). Interannual and interdecadal variability of the north equatorial countercurrent in the western Pacific. *Journal of Geophysical Research: Oceans*, *121*, 7743–7758. https://doi.org/10.1002/2016JC012190

Dee, D. P., Uppala, S. M., Simmons, A. J., Berrisford, P., Poli, P., Kobayashi, S., et al. (2011). The ERA-interim reanalysis: Configuration and performance of the data assimilation system. *Quarterly Journal of the Royal Meteorological Society*, *137*(656), 553–597. https://doi.org/10.1002/qj.828

Emery, W. J., & Thomson, R. E. (2001). *Data analysis methods in physical oceanograhy* (p. 638). Amsterdam: Elsevier.

Fine, R. A., Lukas, R., Bingham, F., Warnar, M., & Gammon, R. (1994). The western equatorial Pacific: A water mass crossroads. *Journal of Geophysical Research*, *99*(C12), 25,063–25,080. https://doi.org/10.1029/94JC02277

Fu, L.-L. (2009). Pattern and velocity of propagation of the global ocean eddy variability. *Journal of Geophysical Research*, *114*, C11017. https://doi.org/10.1029/2009JC005349

Fu, L.-L., & Qiu, B. (2002). Low-frequency variability of the North Pacific Ocean: The roles of boundary-driven and wind-driven baroclinic Rossby waves. *Journal of Geophysical Research*, *107*(C12), 3220. https://doi.org/10.1029/2001JC001131

Gordon, A. L. (1986). Interocean exchanges of thermocline water. *Journal of Geophysical Research*, *91*(C4), 5037–5046. https://doi.org/10.1029/JC091iC04p05037

Gordon, A. L. (2005). Oceanography of the Indonesian seas and their throughflow. *Oceanography*, *18*(4), 14–27. https://doi.org/10.5670/oceanog.2005.01

Gordon, A. L., Huber, B. A., Metzger, E. J., Susanto, R. D., Hurlburt, H. E., & Adi, T. R. (2012). South China Sea throughflow impact on the Indonesian throughflow. *Geophysical Research Letters*, *39*, L11602. https://doi.org/10.1029/2012GL052021

Hsin, Y.-C., & Qiu, B. (2012). Seasonal fluctuations of the surface north equatorial countercurrent (NECC) across the Pacific basin. *Journal of Geophysical Research*, *117*, C06001. https://doi.org/10.1029/2011JC007794

Kashino, Y., Watanabe, H., Herunadi, B., Aoyama, M., & Hartoy, D. (1999). Current variability at the Pacific entrance of the Indonesian Throughflow. *Journal of Geophysical Research*, *104*(C5), 11,021–11,035. https://doi.org/10.1029/1999JC900033

Madden, R. A., & Julian, P. R. (1994). Observations of the 40-50-day tropical oscillation—A review. *Monthly Weather Review*, *122*(5), 814–837. https://doi.org/10.1175/1520-0493(1994)122%3C0814:OOTDTO%3E2.0.CO;2

Marshall, J. C., Adcroft, A., Hill, C., Perelman, L., & Heisey, C. (1997). A finite-volume, incompressible Navier Stokes model for studies of the ocean on parallel computers. *Journal of Geophysical Research*, *102*, 5753–5766.

Masumoto, Y., Kagimoto, T., Yoshida, M., Fukuda, M., Hirose, N., & Yamagata, T. (2001). Intraseasonal eddies in the Sulawesi Sea simulated in an ocean general circulation model. *Geophysical Research Letters*, *28*(8), 1631–1634. https://doi.org/10.1029/2000GL011835

Menemenlis, D., Fukumori, I., & Lee, T. (2005). Using Green's functions to calibrate an ocean general circulation model. *Monthly Weather Review*, *133*(5), 1224–1240. https://doi.org/10.1175/MWR2912.1

Napitu, A. M., Gordon, A. L., & Pujiana, K. (2015). Intraseasonal sea surface temperature variability across the Indonesian Seas. *Journal of Climate*, *28*(22), 8710–8727. https://doi.org/10.1175/JCLI-D-14-00758.1

Potemra, J. T. (2001). The potential role of equatorial Pacific winds on southern tropical Indian Ocean Rossby waves. *Journal of Geophysical Research*, *106*(C2), 2407–2422. https://doi.org/10.1029/1999JC000031

Pujiana, K., Gordon, A. L., Metzger, E. J., & Ffield, A. L. (2012). The Makassar Strait pycnocline variability at 20–40 days. *Dynamics of Atmospheres and Oceans*, *53-54*, 17–35. https://doi.org/10.1016/j.dynatmoce.2012.01.001

Pujiana, K., Gordon, A. L., Sprintall, J., & Susanto, R. D. (2009). Intraseasonal variability in the Makassar Strait thermocline. *Journal of Marine Research*, *67*(6), 757–777. https://doi.org/10.1357/002224009792006115

Qiu, B., & Chen, S. (2010). Interannual-to-decadal variability in the bifurcation of the North Equatorial Current off the Philippines. *Journal of Physical Oceanography*, *40*(11), 2525–2538. https://doi.org/10.1175/2010JPO4462.1

Qiu, B., Chen, S., & Kashino, Y. (1999). Intraseasonal variability in the Indo–Pacific throughflow and the regions surrounding the Indonesian seas. *Journal of Physical Oceanography*, *29*(7), 1599–1618. https://doi.org/10.1175/1520-0485(1999)029%3C1599:IVITIP%3E2.0.CO;2

Qiu, B., Chen, S., & Schneider, N. (2017). Dynamical links between the decadal variability of the Oyashio and Kuroshio extensions. *Journal of Climate*, *30*(23), 9591–9605. https://doi.org/10.1175/JCLI-D-17-0397.1

Qiu, B., & Lukas, R. (1996). Seasonal and interannual variability of the North Equatorial Current, the Mindanao Current and the Kuroshio along the Pacific western boundary. *Journal of Geophysical Research*, *101*(C5), 12,315–12,330. https://doi.org/10.1029/95JC03204

Ray, R. D. (1998). Spectral analysis of highly aliased sea-level signals. *Journal of Geophysical Research*, *103*(C11), 24,991–25,003. https://doi.org/10.1029/98JC02545

Sprintall, J., Gordon, A. L., Koch-Larrouy, A., Lee, T., Potemra, J. T., Pujiana, K., & Wijffels, S. E. (2014). The Indonesian Seas and their role in the coupled ocean-climate system. *Nature Geoscience*, *7*, 487–492.

Sprintall, J., Gordon, A. L., Murtugudde, R., & Susanto, R. D. (2000). A semiannual Indian Ocean forced Kelvin wave observed in the Indonesian seas in May 1997. *Journal of Geophysical Research*, *105*(C7), 17,217–17,230. https://doi.org/10.1029/2000JC900065

Susanto, R. D., Gordon, A. L., Sprintall, J., & Herunadi, B. (2000). Intraseasonal variability and tides in Makassar Strait. *Geophysical Research Letters*, *27*(10), 1499–1502. https://doi.org/10.1029/2000GL011414

Wijffels, S., & Meyers, G. (2004). An intersection of oceanic waveguides: Variability in the Indonesian Throughflow region. *Journal of Physical Oceanography*, *34*(5), 1232–1253. https://doi.org/10.1175/1520-0485(2004)034%3C1232:AIOOWV%3E2.0.CO;2

Wunsch, C., Heimbach, P., Ponte, R., & Fukumori, I. (2009). The global general circulation of the ocean estimated from the ECCO-consortium. *Oceanography*, *22*(2), 88–103. https://doi.org/10.5670/oceanog.2009.41

Zemskova, V. E., White, B. L., & Scotti, A. (2015). Available potential energy and the general circulation: Partitioning wind, buoyancy forcing, and diapycnal mixing. *Journal of Physical Oceanography*, *45*(6), 1510–1531. https://doi.org/10.1175/JPO-D-14-0043.1

Zhang, C. (2005). Madden-Julian oscillation. *Reviews of Geophysics*, *43*, RG2003. https://doi.org/10.1029/2004RG000158

Zhao, J., Li, Y., & Wang, F. (2013). Dynamical responses of the west Pacific North Equatorial Countercurrent (NECC) system to El Niño events. *Journal of Geophysical Research: Oceans*, *118*, 2828–2844. https://doi.org/10.1002/jgrc.20196

Zhuang, W., Qiu, B., & Du, Y. (2013). Low-frequency western Pacific Ocean sea level and circulation changes due to the connectivity of the Philippine Archipelago. *Journal of Geophysical Research: Oceans*, *118*, 6759–6773. https://doi.org/10.1002/2013JC009376